Atmos. Chem. Phys. Discuss., 14, 21285–21314, 2014
www.atmos-chem-phys-discuss.net/14/21285/2014/
doi:10.5194/acpd-14-21285-2014


Atmospheric Chemistry and Physics Discussions



# A new method for measuring the imaginary part of refractive index structure parameter in the urban surface layer

**R. Yuan[1], T. Luo[1], J. Sun[2], Z. Zeng[1], and Y. Fu[1]**

[1]Key Laboratory of the Atmospheric Composition and Optical Radiation, CAS, School of Earth and Space Sciences, University of Science and Technology of China, Anhui, 230026, China
[2]School of Atmospheric Sciences, Nanjing University, Jiangsu, 210093, China

Received: 20 July 2014 – Accepted: 25 July 2014 – Published: 20 August 2014

Correspondence to: R. Yuan (rmyuan@ustc.edu.cn) and T. Luo (luotao@ustc.edu.cn)

Published by Copernicus Publications on behalf of the European Geosciences Union.







## Abstract

Atmospheric refractive index consists of both the real and the imaginary parts. The intensity of refractive index fluctuation is usually expressed as the refractive index structure parameter, whose real part reflects the strength of the atmospheric turbulence while the imaginary part reflects the absorption in the light path. The large aperture scintillometer (LAS) is often used to measure the structure parameter of the real part of atmospheric refractive index, and the sensible and latent heat fluxes can further be obtained, while the influence of the imaginary part is ignored, or thought to be a noise. Based on the expression for the spectrum of the logarithmic light intensity fluctuation caused by the imaginary part of refractive index, new expressions for the logarithmic intensity fluctuation variance and the structure function related to the imaginary part of refractive index are derived. Then a simple expression for the imaginary part of the atmospheric refractive index structure parameter (ARISP) is obtained. It can be conveniently used to measure the imaginary part of the ARISP from LAS. Experiments of light propagation were performed in the urban surface layer and the imaginary part of the ARISP was calculated. The experimental results showed a good agreement with the presented theory. The results also suggested that, the imaginary part of ARISP shows a different variation from the real part of ARISP. For the light with the wavelength of 0.62 μm, the variation of the imaginary part of ARISP is related to both the turbulent transport process and the spatial distribution characteristics of aerosols. Based on the theoretical analysis, it can be expected that the method presented in this study can be applied to measuring the imaginary part of the ARISP caused by the trace gas, if the light wavelength is selected within the corresponding gas absorption region.

## 1 Introduction

In the atmosphere, the line-sight propagating light wave is affected by the scattering and absorption of the turbulence and the aerosol particles. After the light propagates





ACPD
14, 21285–21314, 2014



a distance, the fluctuation of the light intensity is not only related to the inhomogeneous scattering due to the turbulence and particles, but also related to their absorption. According to optical propagating theory (Rao, 2012; Tatarskii, 1961), the scattering is associated with the real part of atmospheric refractive index, and the absorption is associated with the imaginary part. Based on the relationship between the fluctuation of the light intensity on the receiving plane after light propagating a distance and the fluctuation of the real part of atmospheric refractive index (Clifford, 1971; De Bruin and Evans, 2012; Wang et al., 1978), the real part of atmospheric refractive index structure parameter (ARISP) can be deduced. Under the free-convection condition, the real part of ARISP is related to the turbulent transport of temperature and water vapor (Wyngaard et al., 1971), which allows the large aperture scintillometer (LAS) to measure the sensible heat flux and latent heat flux by measuring light intensity fluctuation (Andreas, 1989). When electromagnetic wave propagates in the atmosphere, absorption will inevitably happen, and some mathematical methods can be used to remove the contribution of absorption to scintillation under weak atmospheric absorption conditions (Solignac et al., 2012). However, it is important to understand the role of absorption in observed scintillation under strong atmospheric absorption conditions, such as polluted atmospheric boundary layer or selected atmospheric absorption regions. This study aims to develop a theoretical framework to analyze the absorption's contribution to scintillation, which can be used to derive the imaginary part of ARISP in the urban atmospheric boundary layer from scintillation measurements.

As early as 1983, Filho measured the scintillation spectra from a microwave on a distance of 4.1 km in London city centre area (Filho et al., 1983). The frequency of the microwave is on the side of the 60 GHz oxygen absorption peak, and the wavelength (5.4 mm) is far larger than the aerosol size. Results showed that the lower corner frequency predicted by Ott and Thompson Jr. (Ott and Thompson Jr., 1978) is a good approximation for the enhancement of the scintillations due to the $O_2$ absorption. Nieveen et al. (Nieveen et al., 1998) obtained the imaginary part of the ARISP of about $4.1 \times 10^{-24}$ m$^{-2/3}$ at a pasture site based on the scintillation data over 248 m distance at





ACPD
14, 21285–21314, 2014



a wavelength of 0.940 µm, which is inside a water vapour absorption band. The experiment did not measure the aerosol information. Thus the absorption by aerosol cannot be identified. In those studies, the imaginary part of the ARISP was obtained by the lower corner frequency in the spectral densities of light intensity fluctuations. But it is difficult to objectively identify the lower corner frequency due to the variations in the low frequencies of these spectral densities.

Limited research has been conducted on the contribution to the intensity fluctuation of light wave by aerosol absorptions. The possible reason is that, the aerosol concentrations are low in lots of areas and thus the contribution is too small. However, many developing countries are suffering increasing aerosol pollution with high fraction of soot contributions. For example, many cities in China experience more and more serious fog and haze conditions, which strongly affect the visibility and radiation (Ding and Liu, 2014). The soot aerosols have strong and broad absorptions. A few studies have been performed to measure the mean imaginary part of aerosol refractive index (Raut and Chazette, 2008; Zhang et al., 2013), which indicates that the temporal and spatial distributions of the imaginary refractive index are highly variable. Their inhomogenities can be described by the imaginary part of the ARISP. Therefore, the knowledge of the imaginary part of the ARISP can be used to further understand the temporal and spatial distributions of the imaginary refractive index and the aerosol transportation.

Based on the proposed theoretical framework and the LAS experiments at the visible band in the urban surface layer, a new objective method is developed to obtain the imaginary part of the ARISP by combining the light fluctuation variances and structure functions including the contribution of imaginary refractive index. The experiments were performed in Hefei, China. The results show that the imaginary part of the ARISP can be reliably derived by this method.

Section 2 presents the theoretical framework. Section 3 describes the experiment. Section 4 gives experimental results, which show that the proposed approach is capable of providing the characteristics of the imaginary part of the ARISP in the urban boundary layer. At the last, a brief conclusion is presented.





ACPD
14, 21285–21314, 2014



## 2 Theory

When the light wave propagates through a distance in the atmosphere, the light intensity fluctuates on the receiving plane. A theoretical framework is presented here to connect the spatial and temporal spectra of log-intensity and the variances and the structure function of log-intensity with the real and imaginary parts of refractive index. Based on this framework, the imaginary part of the ARISP can be directly obtained from LAS measurements.

### 2.1 The spatial spectrum of the log-intensity and the spectrum of refractivity index fluctuation

For a planar or a spherical wave in the slowly varying turbulence field, the two-dimensional log-intensity spectrum is (Filho et al., 1983),

$$F_{\ln I}(\kappa, L) = 4F_{\chi}(\kappa, L) = 8\pi k^2 \int_0^L \left\{ \Phi_{n,\mathrm{Re}}(\kappa)\sin^2(\theta) + \Phi_{n,\mathrm{Im}}\cos^2(\theta) + \Phi_{n,\mathrm{IR}}\sin(2\theta) \right\} \mathrm{d}z \quad (1)$$

In Eq. (1), $\theta$ is $\kappa^2 z(L-z)/2kL$ for spherical wave, or $\kappa^2(L-z)/2k$ for plane wave (in this study, only the spherical wave is considered), $\kappa$ is the wave number of the two-dimensional log-intensity spectrum and $k$ is the wave number of a spherical wave, $z$ is the position for wave propagating, $L$ is the length of propagation path; $\Phi_n$ is the spectrum of the refractive index, here the subscript $n$ denotes refractive index, the subscripts Re and Im denote the real and the imaginary part of the refractive index respectively, and the subscript IR denotes correlation between the real part and the imaginary part. In the following analysis, it's assumed that the fluctuations in the real and imaginary parts of refractive index are not correlated (Filho et al., 1983), and thus the joint part can be neglected.

Assuming that the absorption media in the atmosphere and the temperature are conservative and passive scalars with their sources at the surface, $\Phi_{n,\mathrm{Re}}$ and $\Phi_{n,\mathrm{Im}}$





ACPD
14, 21285–21314, 2014



have the same form. The widely used von Karman spectrum form is adopted in the study (Andrews and Phillips, 2005), which gives

$$\Phi_{n,\mathrm{Re}}(\kappa) = 0.033 C^2_{n,\mathrm{Re}} \left(\kappa^2 + \frac{1}{L_0^2}\right)^{-\frac{11}{6}} e^{-\frac{\kappa^2 l_0^2}{5.92^2}} \tag{2}$$

$$\Phi_{n,\mathrm{Im}}(\kappa) = 0.033 C^2_{n,\mathrm{Im}} \left(\kappa^2 + \frac{1}{L_0^2}\right)^{-\frac{11}{6}} e^{-\frac{\kappa^2 l_0^2}{5.92^2}} \tag{3}$$

Here, $C^2_{n,\mathrm{Re}}$ and $C^2_{n,\mathrm{Im}}$ are the real and imaginary parts of ARISP respectively. $L_0$ is the outer scale of turbulence, and $l_0$ is the inner scale of turbulence. Although some measurements revealed that the turbulence often show anisotropic characteristics (Consortini et al., 1970; Yuan et al., 2014), the isotopic turbulence assumption will still be used in this paper.

### 2.2 One dimensional temporal spectrum of the log-intensity fluctuation

The one dimensional spatial spectrum can be derived from the integration of Eq. (1) by assuming the isotopic turbulence, and then it can be converted to temporal spectrum according to the Taylor frozen hypothesis. Considering the aperture-smoothing effects, the temporal spectrum caused by the real part can be expressed as (Nieveen et al., 1998; Clifford, 1971),

$$W_{\ln I,\mathrm{Re}}(f) = 64\pi^2 k^2 \int_0^L \mathrm{d}z \int_{2\pi f/v}^{\infty} \Phi_{n,\mathrm{Re}}(\kappa) \sin^2\left[\frac{\kappa^2 z(L-z)}{2kL}\right] [(\kappa v)^2 - (2\pi f)^2]^{-1/2} \cdot \left[\frac{2J_1\left(\frac{D_t \kappa z}{2L}\right)}{D_r \kappa z/2L}\right]^2 \left[\frac{2J_1\left(\frac{D_t \kappa (L-z)}{2L}\right)}{D_t \kappa (L-z)/2L}\right]^2 \kappa \mathrm{d}\kappa \tag{4}$$





ACPD
14, 21285–21314, 2014



Here, $D_t$ is the transmitting aperture diameter; $D_r$ is receiving aperture diameter ($D_t$ and $D_r$ are usually same for a LAS), $v$ is the transverse wind speed. $J_1$ is the first order Bessel function.

Similarly, the temporal spectrum caused by the imaginary part could be derived as (Nieveen et al., 1998; Clifford, 1971),

$$W_{\ln/,\mathrm{Im}}(f) = 64\pi^2 k^2 \int_0^L \mathrm{d}z \int_{2\pi f/v}^{\infty} \mathrm{d}\kappa\kappa\Phi_{n,\mathrm{Im}}(\kappa)\cos^2\left[\frac{\kappa^2 z(L-z)}{2kL}\right][(\kappa v)^2 - (2\pi f)^2]^{-1/2} \cdot \left[\frac{2J_1\left(\frac{D_r\kappa z}{2L}\right)}{D_r\kappa z/2L}\right]^2 \left[\frac{2J_1(\frac{D_t\kappa(L-z)}{2L})}{D_t\kappa(L-z)/2L}\right]^2 \quad (5)$$

Figure 1 gives a case of the temporal spectrum of the log-intensity calculated with parameters of $C^2_{n,\mathrm{Re}} = 9.5\times10^{-15}\,\mathrm{m}^{-2/3}$, $C^2_{n,\mathrm{Im}} = 4.0\times10^{-24}\,\mathrm{m}^{-2/3}$, $L_0 = 27.1\,\mathrm{m}$, $L = 960\,\mathrm{m}$, $D_t = D_r = 0.18\,\mathrm{m}$, and $v = 1.3\,\mathrm{m\,s}^{-1}$ (how to obtain $C^2_{n,\mathrm{Im}}$ and $L_0$ will be introduced in the following text). The dashed line is the temporal spectrum of the log-intensity contributed by the real part of the refractive index, which reaches a plateau at frequencies lower than 3 Hz. The spectral density of the plateau part ($\mathrm{WP}_{\ln/,\mathrm{Re}}$) could be numerically calculated as

$$\mathrm{WP}_{\ln/,\mathrm{Re}} = 1.04L^3 D_t^{-2/3} D_r^{-2/3} C^2_{n,\mathrm{Re}} v^{-1} \quad (6)$$

The solid line represents the temporal spectrum of the log-intensity related to the imaginary part of refractive index. The sum of both real and imaginary part contributions, presented as the circles in Fig. 1, corresponds to the measured spectrum of the log-intensity from LAS experiments. The contribution of the imaginary part of the refractive index is mainly at the lower frequencies according to Eq. (5). At the low frequencies, the spectral density contributed by the real part of the refractive index is small





ACPD
14, 21285–21314, 2014



compared to the measured spectrum, which allows the contribution of the imaginary part of the refractive index to be determined from the measurements.

### 2.3 The log-intensity variances caused by the real and imaginary part of the refractive index

The log-intensity fluctuation can be decomposed into the ensemble average ($A_0$), the slow fluctuation (e.g. low frequency) caused by the imaginary part of the refractive index ($\tilde{A}$) and the quick fluctuation (e.g. high frequency) caused by real part of the refractive index ($A'$), as

$$\ln I = A_0 + \tilde{A}(r) + A'(r) \tag{7}$$

Assuming that the variances caused by the real and imaginary parts are independent, the log-intensity variance can be derived as $\sigma^2_{\ln I} = \overline{[A - \overline{A}]^2} = \overline{[\tilde{A} - \overline{\tilde{A}}]^2} + \overline{[A' - \overline{A'}]^2}$, and consequently,

$$\sigma^2_{\ln I} = \sigma^2_{\ln I,\mathrm{Re}} + \sigma^2_{\ln I,\mathrm{Im}} \tag{8}$$

Based on Eq. (8), the measured log-intensity fluctuation variance is the sum of variances at low and high frequencies, which could be determined by integrating Eqs. (4) and (5) respectively.

Integrating of Eq. (4) gives the log-intensity variance caused by the real part of the refractive index (Wang et al., 1978), which is

$$\sigma^2_{\ln I,\mathrm{Re}} = 0.89 C^2_{n,\mathrm{Re}} L^3 D_\mathrm{t}^{-7/6} D_\mathrm{r}^{-7/6} \tag{9}$$

In Eq. (9), the variables $L$, $D_\mathrm{t}$ and $D_\mathrm{r}$ are constants, so $\sigma^2_{\ln I,\mathrm{Re}}$ depends only on the real part of the ARISP, $C^2_{n,\mathrm{Re}}$, which can be expressed as:

$$C^2_{n,\mathrm{Re}} = 1.12 \sigma^2_{\ln I,\mathrm{Re}} L^{-3} D_\mathrm{t}^{7/6} D_\mathrm{r}^{7/6} \tag{10}$$





ACPD
14, 21285–21314, 2014



Equation (10) is the common-used equation for LAS measurements and data analyses (Wang et al., 1978).

Combining Eqs. (6) and (9), the transverse velocity could be obtained as

$$v = \frac{1.16 D_t^{1/2} D_r^{1/2} \sigma^2_{\ln I,\mathrm{Re}}}{\mathrm{WP}_{\ln I,\mathrm{Re}}} \tag{11}$$

Similarly, integrating of Eq. (5) provides the log-intensity variance caused by the imaginary part of the refractive index as

$$\sigma^2_{\ln I,\mathrm{Im}} = 2.95 C^2_{n,\mathrm{Im}} k^2 L_0^{5/3} L \tag{12}$$

When fixing $L$ and $k$, $\sigma^2_{\ln I,\mathrm{Im}}$ depends not only on the imaginary part of the ARISP ($C^2_{n,\mathrm{Im}}$), but also on the outer scale $L_0$. Therefore, $C^2_{n,\mathrm{Im}}$ cannot be derived by Eq. (12) only. Determining $C^2_{n,\mathrm{Im}}$ will be further discussed in the next section.

### 2.4 The structure function of the log-intensity fluctuations

The two-point log-intensity correlation moment ($B_{\ln I}(\rho)$) with a distance $\rho$ is defined as (Ishimaru, 1997)

$$B_{\ln I}(\rho) = 2\pi \int_0^\infty F_{\ln I}(\kappa, 0) J_0(\kappa\rho) \kappa \mathrm{d}\kappa \tag{13}$$

Here, $J_0$ is the zero-order Bessel function. With the Eq. (1), the correlation moment related to the real part of the refractive index can be expressed as (Ishimaru, 1997):

$$B_{\ln I,\mathrm{Re}}(\rho) = 16\pi^2 k^2 \int_0^L \mathrm{d}z \int_0^\infty \Phi_{n,\mathrm{Re}} \sin^2(\theta) J_0(\kappa\rho) \kappa \mathrm{d}\kappa \tag{14}$$





ACPD
14, 21285–21314, 2014



Similarly, the correlation moment contributed by the imaginary part of the refractive index can be written as:

$$B_{\ln I,\mathrm{Im}}(\rho) = 16\pi^2 k^2 \int_0^L \mathrm{d}z \int_0^\infty \Phi_{n,\mathrm{Im}} \cos^2(\theta) J_0(\kappa\rho)\kappa \mathrm{d}\kappa \tag{15}$$

According to the relationship between the correlation moment and structure function, the structure function can be derived as

$$D_{\ln I}(\rho) = 4\pi \int_0^\infty F_{\ln I}(\kappa, 0)[1 - J_0(\kappa\rho)]\kappa \mathrm{d}\kappa \tag{16}$$

When considering the aperture smoothing effect, the real part of the structure function becomes,

$$D_{\ln I,\mathrm{Re}}(\rho) = 32\pi^2 k^2 \int_0^L \mathrm{d}z \int_0^\infty \Phi_{n,\mathrm{Re}} \sin^2(\theta)[1 - J_0(\kappa\rho)]\kappa \mathrm{d}\kappa \left[\frac{2J_1\left(\frac{D_r \kappa z}{2L}\right)}{D_r \kappa z/2L}\right]^2 \left[\frac{2J_1\left(\frac{D_t \kappa (L-z)}{2L}\right)}{D_t \kappa (L-z)/2L}\right]^2 \tag{17}$$

With further derivations, the following simplified relationships are validated under different conditions:

$$D_{\ln I,\mathrm{Re}}(\rho) = 14.8 C_{n,\mathrm{Re}}^2 L^3 D_t^{-13/6} D_r^{-13/6} \rho^2 \qquad \rho \ll D_t \text{ (or } D_r) \tag{18a}$$

$$D_{\ln I,\mathrm{Re}}(\rho) = 4.3 C_{n,\mathrm{Re}}^2 L^3 D_t^{-11/6} D_r^{-11/6} \rho^{4/3} \qquad \rho < D_t \text{ (or } D_r) \tag{18b}$$

$$D_{\ln I,\mathrm{Re}}(\rho) = 1.78 C_{n,\mathrm{Re}}^2 L^3 D_t^{-7/6} D_r^{-7/6} \qquad \rho \geq D_t \text{ (or } D_r) \tag{18c}$$

The $D_{\ln,I,\mathrm{Re}}$ relates to the diameters of transmitting and receiving aperture. The dashed line in Fig. 2 shows the log-intensity structure function related to the real part





ACPD
14, 21285–21314, 2014



of the refractive index calculated with the same parameters as in Fig. 1. As shown in Fig. 2, when $\rho$ is relatively small, $D_{\ln/,\mathrm{Re}}$ increases with increasing $\rho$, and it becomes saturated when $\rho$ reaches to the size of the diameter of LAS aperture, which equals to two times of the log-intensity variance caused by the $C^2_{n,\mathrm{Re}}$ (the right side of Eq. 18c is two times the right side of Eq. 9).

Similarly, the log-intensity structure function caused by the imaginary part of the refractive index is

$$D_{\ln/,\mathrm{Im}}(\rho) = 32\pi^2 k^2 \int_0^L \mathrm{d}z \int_0^\infty \Phi_{n,\mathrm{Im}}(\kappa)\cos^2(\theta)[1 - J_0(\kappa\rho)]\kappa \mathrm{d}\kappa \cdot \left[\frac{2J_1\left(\frac{D_r\kappa z}{2L}\right)}{D_r\kappa z/2L}\right]^2 \left[\frac{2J_1\left(\frac{D_t\kappa(L-z)}{2L}\right)}{D_t\kappa(L-z)/2L}\right]^2 \quad (19)$$

The following simplified relationships could be derived through further derivations:

$$D_{\ln/,\mathrm{Im}}(\rho) = 8.5C^2_{n,\mathrm{Im}}k^2 L\rho^{5/3} \qquad (D_t \text{ (or } D_r) < \rho \ll L_0) \quad (20a)$$

$$D_{\ln/,\mathrm{Im}}(\rho) = 2.95C^2_{n,\mathrm{Im}}k^2 L\rho^{7/6}L_0^{1/2} \qquad (\rho \lesssim L_0) \quad (20b)$$

Here, a relationship is not given in terms of $\rho$ when $\rho$ is less than $D_t$ (or $D_r$), because under this condition contribution to the structure function caused by $C^2_{n,\mathrm{Im}}$ is much less than the contribution of $C^2_{n,\mathrm{Re}}$, which is clearly illustrated in Fig. 2. The solid line in Fig. 2 shows the structure function caused by $C^2_{n,\mathrm{Im}}$ and the hollow circle line is the sum of the contribution of $C^2_{n,\mathrm{Im}}$ and $C^2_{n,\mathrm{Re}}$. It is obvious that contribution to the structure function caused by $C^2_{n,\mathrm{Im}}$ is much less than by $C^2_{n,\mathrm{Re}}$ when $\rho$ is less than $D_t$ (or $D_r$). When $\rho$ is larger than the aperture diameter and far smaller than the outer scale, Eq. (20) indicates that the $D_{\ln/,\mathrm{Im}}$ depends only on $C^2_{n,\mathrm{Im}}$. However, the uncertainty in calculating





ACPD
14, 21285–21314, 2014



the imaginary part of the log-intensity structure function is relatively large because the contribution from $C^2_{n,\mathrm{Re}}$ dominates when $\rho$ is smaller than the outer scale $L_0$. When $\rho$ is close to the outer scale $L_0$, the contribution from $C^2_{n,\mathrm{Im}}$ can be easily identified, as shown in Fig. 2. Therefore, to reduce the noise and select a proper $\rho$ ($\rho$ should be close to $L_0$ but less than $L_0$), the Eq. (20b) can be used to determine $C^2_{n,\mathrm{Im}}$.

Combining Eq. (20b) and (12), we get

$$C^2_{n,\mathrm{Im}} = \frac{1}{2.95} \frac{D^{10/7}_{\ln I,\mathrm{Im}}}{\left(\sigma^2_{\ln I,\mathrm{Im}}\right)^{3/7} k^2 L \rho^{5/3}} \tag{21}$$

$$L_0 = \left(\sigma^2_{\ln I,\mathrm{Im}} / D_{\ln I,\mathrm{Im}}\right)^{6/7} \rho \tag{22}$$

Equations (21) and (22) will be used to calculate the imaginary part of the ARISP $C^2_{n,\mathrm{Im}}$ and the outer scale $L_0$.

Based on the previous spectrum analysis, when $\rho$ is larger than the aperture diameter, the contribution to the structure function from $C^2_{n,\mathrm{Re}}$ becomes saturated, which equals to two times of the log-intensity variance caused by $C^2_{n,\mathrm{Re}}$. Therefore, the structure function caused by $C^2_{n,\mathrm{Im}}$ can be derived by subtracting two times of the log-intensity variance caused by $C^2_{n,\mathrm{Re}}$ from the measured one.

According to Eq. (7), the structure function could be presented as $D_{\ln I}(\rho) = [\tilde{A}(r+\rho) + A'(r+\rho) - \tilde{A}(r) - A'(r)]^2$, and further as

$$D_{\ln I}(\rho) = D_{\ln I,\mathrm{Im}}(\rho) + D_{\ln I,\mathrm{Re}}(\rho) \tag{23a}$$

$$D_{\ln I}(\rho) = D_{\ln I,\mathrm{Im}}(\rho) + 2\sigma^2_{\ln I,\mathrm{Re}}(\rho) \quad \rho \geq D_t \text{ (or } D_r) \tag{23b}$$

For measurements at one point, the transform from space to time could be performed according to the Taylor hypothesis, i.e.$\rho = v\tau$ ($\tau$ is the delay time), so we have,

$$D_{\ln I,\mathrm{Im}}(v\tau) = D_{\ln I}(v\tau) - 2\sigma^2_{\ln I,\mathrm{Re}} \quad v\tau \geq D_t \text{ (or } D_r) \tag{24}$$





ACPD
14, 21285–21314, 2014



Equation (24) will be used to calculate the imaginary part of the structure function.

## 3 Experiment and data process

In this section, the description of the experiments and the steps of data process according to the theory presented above will be given.

### 3.1 Description of the experiments

The light propagation experiments were conducted in the campus of the University of Science and Technology of China (USTC). Figure 3a shows the southern area of the Hefei city, and Fig. 3b shows the experiment site in the USTC campus. The experiment site represents a typical urban underlying surface. The campus is surrounded by heavy traffic urban roads. Two main roads are located at the west and north, and a viaduct is overhead the western road. Four-story buildings and trees occupied most of the campus, with a mean height of 15 m (this height is treated as the reference plane). The experiments were carried out between the 55 m-high building (symbol A in Fig. 3b) and the 62 m-high building (symbol B in Fig. 3b), which locate at the southernmost and northernmost of the campus, with a distance of 960 m between them. The transmitter was located at the southern building and the receiver was located at the northern building with laser path along the south–north direction. The measurements were performed respectively at the 10th and 12th floor of the two buildings, with heights of 18.5 and 24.5 m above the reference plane. For typical LAS measurements, the height is a very important physical quantity and should be carefully measured and calibrated (Evans and De Bruin, 2011). However, in this study, quantitatively heat flux analyses are not needed, therefore, the measurement heights here are simply referred to the reference plane representing the urban canopy layer.

A meteorology tower (symbol C in Fig. 3b) with the top 18 m above the reference plane is located near the light path. The sensors for wind speed, wind direction,





ACPD
14, 21285–21314, 2014



temperature and humidity were mounted at 3 levels on the tower, of which the uppermost level is at the top of the tower. The meteorological data were sampled every one minute and averaged and saved every 20 min. These measurements are used to derive the stability near the surface. A Double-Point temperature fluctuation sensor was installed at the top of the tower. The Double-Point temperature fluctuation sensor is a widely used method to measure the temperature structure parameter (Yuan et al., 2000; Pant et al., 1999). Two thermal-resistances were inserted into the two arms of an electric bridge with about 0.8 m apart, and then the temperature differences were measured and processed to provide the temperature structure parameter. The temperature structure parameters measured by the Double-Point temperature fluctuation sensor were converted to the real part of ARISP to compare with the LAS measurements. The temperature differences were sampled at 100 Hz, and the real part of ARISP was calculated and saved every 20 min.

The LAS is a copy of the instrument conceived by Ting-i Wang et al. (Wang et al., 1978) and built at USTC. The transmitting and receiving aperture diameters of the LAS used in this measurement are 0.18 m. The light source is a light emitting diode (LED) modulated at 116 kHz. The wavelength is at 0.620 µm, at which the absorption is mainly caused by aerosol comparing to the weak $O_3$ absorption (Brion et al., 1998; Lou et al., 2014; Nebuloni, 2005). The emitted light is converged by the transmit lens and propagate over 960 m to the receiver.

A photo detector, which is located at the focus of the receiving lens, converted light intensities to electrical signals, which can be demodulated and amplified by an amplifier. The bandwidth of the amplifier is 0.002–250 Hz. The output signal is sampled at a frequency of 500 Hz. The data files are saved at 20 min blocks.

There are seven visibility measurement sites near the experiment field. The visibility data is available every 30 min. The measurements from these sites agree well with each other, which mean the visibility in our experiment field can be represented by measurements at these sites. In this study, we use the visibility measurements at 6 m





ACPD
14, 21285–21314, 2014



height from the nearest site, which is about 3 km away from our experiment site and marked as the symbol P in Fig. 3a.

### 3.2 Data analysis method and examples

According to the theory presented in the Sect. 2, the real and the imaginary parts of the ARISP, the transverse wind speed and the turbulence outer scale can be retrieved and calculated from LAS measurements.

Here, the results of the LAS observations at 15 January 2014, 08:30 LT are presented. The LAS observations are collected at 24.5 m above the reference plane with the wind speed of 1.1 m $s^{-1}$ and the wind direction of 86° at 18 m and the visibility of 6.0 km. The calculated $L_{MO} = -11$ m ($L_{MO}$ is the Obukhov length) indicates the atmosphere in the surface layer was unstably stratified.

Two methods are tested for calculating the energy at low and high frequencies. The first one is the time-delay autocorrelation method, and the time-delay autocorrelation function $C_{\ln I}$ with a delay time $i\Delta t$ ($\Delta t$ is the sample interval, $i$ is the data indexes) can be expressed as:

$$C_{\ln I}(i \cdot \Delta t) = \frac{1}{N} \sum_{j}^{N-1} \ln I(j) \cdot \ln I(i - j) \tag{25}$$

Here, $j$ is also the data indexes; $N$ is the length of the data; the delay time $i\Delta t$ is denoted as $\tau$ in Fig. 4. Figure 4a shows the results for the example case. The $x$ axis is the delay time $\tau$, and the $y$ axis is the time-delay autocorrelation. At the upper right corner of Fig. 4a, a partial enlarged plot shows two asymptotic lines with intersection point at (0.07 s, $2.59 \times 10^{-4}$). Because $\ln I$ is a non-dimensional variable, the $C_{\ln I}$ is certainly a non-dimensional variable. Figure 4a shows that the autocorrelation has the maximum of $6.68 \times 10^{-4}$ when $\tau$ is close to zero. Thus the total variance of the log-intensity is $6.68 \times 10^{-4}$. When $\tau$ is smaller than 0.07 s, the autocorrelation decreases rapidly with increasing $\tau$, which is attributed to the real part of the refractive index





ACPD
14, 21285–21314, 2014



because the real part corresponds to the high frequent fluctuation (William et al., 2007). When $\tau$ is larger than 0.07 s, the autocorrelation decreases slowly with increasing $\tau$, which is attributed to the imaginary part of the refractive index. Therefore, the horizontal asymptotic line indicates that the log-intensity variance caused by the imaginary part of the refractive index is $2.59 \times 10^{-4}$. The difference of the total variances and the variance caused by the imaginary part is the variance ($4.09 \times 10^{-4}$) contributed by the real part of the refractive index.

Using Eqs. (10) and (11), $C^2_{n,\mathrm{Re}}$ equals $9.5 \times 10^{-15}\,\mathrm{m}^{-2/3}$ and the transverse wind speed is $1.3\,\mathrm{m\,s}^{-1}$. For the transverse wind speed, $\mathrm{WP}_{\mathrm{ln}/,\mathrm{Re}}$ in Eq. (11) is required and will be inferred in the following part. There are many methods to retrieve the wind speed by LAS (van Dinther et al., 2013). Equation (11) is more simple and stable than the other approaches according to our results.

After calculating the energy at high frequencies, the structure function caused by the imaginary part of the refractive index can be obtained by Eq. (24) and is shown as hollow circles in Fig. 4b. It can be seen that, when the delay time is close to 1 s, the calculated structure function has very large variations, because contribution caused by the imaginary part of the refractive index is almost the same order as the real part and the subtraction results in a large variation; when the delay time is larger than 10 s, the structure function follows the 7/6 power law as suggested by Eq. (20b). Thus $C^2_{n,\mathrm{Im}} = 4.0 \times 10^{-24}\,\mathrm{m}^{-2/3}$ and $L_0 = 27.1$ m can be derived from Eqs. (21) and (22). With these parameters, the structure function can be calculated with Eq. (19), which is presented as the solid line in Fig. 4b. Meanwhile, the structure function calculated with Eq. (20b) is shown as the dashed line. As shown in Fig. 4b, the simplified relationship given by Eq. (20b) could predict the structure function well when $\tau$ is within 10–50 s.

Figure 4c shows the comparison between the log-intensity fluctuation power spectrum and the theoretical prediction. The measurements agree well with the theoretical prediction except that measurements at high frequencies are higher than theoretical predications, which may be caused by measurement noises. With their different contributions to high and low frequency energy, the energies caused by real and imaginary





ACPD
14, 21285–21314, 2014



part of the refractive index can be obtained by analyzing the spectrum of scintillation. As shown in Fig. 4c, the spectrum density of the plateau part at the frequency of about 1 Hz is $WP_{ln/,Re} = 6.3 \times 10^{-5}$. The energy higher than $WP_{ln/,Re}$ at the lower frequencies is contributed by the imaginary part of the refractive index. With the measured spectrum, the energy at high and low frequencies can be calculated as $4.07 \times 10^{-4}$ and $2.49 \times 10^{-4}$ respectively, which agree well with those determined by the delay autocorrelation method.

Figure 4d shows the log-intensity structure function caused by the real part of the refractive index as a function of the delay time for $\tau$ less than 0.1 s. The circles represent the measurements, and the solid and dashed lines are theoretical calculations with Eqs. (17) and (18b) separately. It shows clearly that the measurements are consistent with the theoretical predictions.

## 4 Results

### 4.1 Comparisons between LAS and meteorology tower measurements

To ensure the reliability of our LAS experiments, the real part of the ARISP and transverse wind speed from the LAS measurements are compared with independent measurements from the meteorology tower. The LAS transmitter and the receiver were installed at the height of 18.5 m, which is close to the mounting height (18.0 m) of cup anemometer and the Double-Point temperature fluctuation sensor. The comparison experiments were conducted during 26–29 December 2013, during which the visibility was more than 10 km.

Figure 5a show the comparison of the real part of the ARISP derived from the Double-Point temperature fluctuation sensor and the LAS based on Eq. (10). The slope of the regression line is 1.09 and the correlation coefficient is 0.95. Considering the potential differences between short-range and long-path integrated measurements, this agreement is very good. However, when the turbulent intensity is weak,





ACPD
14, 21285–21314, 2014



LAS measurements are slightly larger than those from the Double-Point temperature fluctuation sensor, which may be due to the contribution of aerosol to the real part of the ARISP during night time.

The transverse wind speed can easily be calculated from the LAS with Eq. (10) ($v$ in $y$ axis of Fig. 5b) and compared with cup anemometer measurements ($U_{\perp}$ in $x$ axis of Fig. 5b) as presented in Fig. 5b. The slope of the regression line is 0.99 and the correlation coefficient is 0.96. The statistics indicate that the overall agreement is good. The transverse wind speeds from LAS are slightly larger than those from the cup anemometer under low wind speed conditions.

### 4.2 Diurnal variations

As a case study, diurnal variations of the real and imaginary parts of the ARISP as well as the visibility, wind speed and direction observed during 15–16 January 2014 are presented. The LAS observations are performed at the height of 24.5 m. The temporal spectrum and structure function of logarithmic light intensity during these two days are shown in Fig. 6a and b, respectively. Figure 6a clearly shows that the high frequency part of temporal spectrum ($\log(f) > -2$) has a pronounced diurnal cycle with large value at noon. But it is not the case for the low frequency part. In Fig. 6b, the structure function of logarithmic light intensity has a pronounced diurnal cycle within the whole scale range with large value at noon and small value during night time.

Based on the theoretical framework presented in Sect. 2, the derived real and imaginary parts of the ARISP are shown in Fig. 7a and b. The visibility, wind speed and direction are also shown in Fig. 7c and d, respectively. Figure 7a shows that the real part of the ARISP has a typical diurnal characteristics of the atmospheric boundary layer turbulence (Stull, 1988). The real part of the ARISP increases gradually after sunrise, then reaches the maximum at noon and approaches to the minimum after sunset. But for the temporal evolution the imaginary part of the ARISP displays a different pattern than the real part. The maximum of the imaginary part of the ARISP occurred on 15 January 2014, 09:00 LT, and on 16 January 2014, 12:00 LT. However, there are also





ACPD
14, 21285–21314, 2014



the large variations of the imaginary part of the ARISP during the other periods. Three of such large variations are labeled as A, B and C in Fig. 7b. Figure 7c shows that visibility in daytime exceeds about 8 km and is less than 8 km during nighttime. The relative humidity during the two days was less than 60 %, so the variation of visibility is mainly caused by near surface aerosol variations associated with aerosol sources and vertical transportation. During the two days, minimal near surface visibility typically occur around 06:00 LT.

Figure 7d shows weak diurnal variations in wind speed and direction. The prevailing direction of the wind throughout the two days is between east and southeast, except large variation of wind direction after 16 January 2014, 12:00 LT. $C^2_{n,\mathrm{Im}}$ started to increase gradually on 15 January 2014, 06:00 LT, and reached maximum at 09:00 LT. Figure 7a and b shows that the increase of $C^2_{n,\mathrm{Im}}$ was earlier than $C^2_{n,\mathrm{Re}}$. Figure 7d shows that wind speeds increase from about 0.5 m s$^{-1}$ at 06:00 LT to about 2.5 m s$^{-1}$ at 10:00 LT. The increase of $C^2_{n,\mathrm{Im}}$ was almost simultaneous with wind speed increase on 16 January 2014. The variations of $C^2_{n,\mathrm{Im}}$ was almost following the variations of $C^2_{n,\mathrm{Re}}$ in the morning. These correlations suggest that $C^2_{n,\mathrm{Im}}$ are affected by both $C^2_{n,\mathrm{Re}}$ and wind speed. It is known that $C^2_{n,\mathrm{Re}}$ and wind associate with convective and shear turbulence respectively. This indicates that turbulence controls $C^2_{n,\mathrm{Im}}$ as expected. However, after $C^2_{n,\mathrm{Im}}$ reached maximum on 15 January 2014, 09:00 LT $C^2_{n,\mathrm{Im}}$ decreased gradually while $C^2_{n,\mathrm{Re}}$ still increased. This situation can be explained by the variation of visibility, which still increased after 09:00 LT, implying lower aerosol concentration. This suggests that the variation of $C^2_{n,\mathrm{Im}}$ is also linked with aerosol variations. The moments A and C correspond with sudden wind direction changes and local rush hours with traffic jam (a strong source of local aerosol production). At point B, $C^2_{n,\mathrm{Im}}$ increased simultaneously with $C^2_{n,\mathrm{Re}}$. The peak values at A, B and C suggest that $C^2_{n,\mathrm{Im}}$ are controlled by both turbulence and aerosol distributions.





ACPD
14, 21285–21314, 2014



## 5 Conclusions and discussion

Based on the theory of light propagation, the fluctuation of logarithmic light intensity depends on both the real and the imaginary parts of the ARISP. Then the relationships among the imaginary part of the ARISP, variance of scintillation and structure function of logarithmic light intensity are deduced, and the expression of the imaginary part of the ARISP is obtained.

Experiments of light propagation through urban surface layer were conducted. The real part of the ARISP and transverse wind speed were obtained using the scintillation data. In the meantime, the real part of the ARISP was measured by the Double-Point temperature fluctuation sensor, and the wind speed and direction were also measured using the cup anemometer. The results show good agreement between the LAS and other methods. The calculated real part of the ARISP displays normal diurnal variation characteristics over urban overlying surface, which coincides the diurnal variation of turbulence strength.

Based on the deduced expressions, the imaginary part of the ARISP was calculated. Results showed good agreement with the theory. The diurnal variation of imaginary part of the ARISP does not show the same trend as that of the real part. By analyzing the two-day variation of the imaginary part of the ARISP together with variations of the real part of the ARISP, visibility, wind speed and direction, we can find that the imaginary part of the ARISP may be influenced by both turbulence and aerosol concentration.

In this study, the wavelength of the used light source is 0.62 µm, and the light attenuation is mainly made by aerosol, so the imaginary part of the ARISP is influenced by turbulence and aerosol distribution. However, the presented method for the imaginary part of the ARISP should be valid for any other wavelength for measurements of gas absorption.

Because the measurement site is in Hefei city with a population of about 3 500 000, vehicles of more than 500 000. For the cities similar to Hefei, for example Helsinki, Finland, vehicles are important pollution source (Jarvi et al., 2009). The variation of





ACPD
14, 21285–21314, 2014



the imaginary part of the ARISP with time has similar trend to the variation of aerosol flux (Ripamonti et al., 2013). Their large value happens at rush hours of 09:00 LT and 18:00 LT, and the two variables vary significantly with wind direction. Evidence shows that the imaginary part of the ARISP is an important variable which can provide information about aerosol. The results in this study indicate that the imaginary part of the ARISP can be easily derived from the LAS measurements. What information of aerosol does the imaginary part of the ARISP represent, flux or concentration, should be investigated further.

*Acknowledgements.* This study was supported by the National Natural Science Foundation of China (40975006, 41230419, 91337213 and 41075041) and the Jiangsu Provincial Collaborative Innovation Center of Climate Change. Thanks will also be given to G. Liu, Y. Yuan, Y. Wang, G. Liu, C. Shi and R. Zhou for their help in collecting data and preparing experiments.

## References

Andreas, E. L.: Two-wavelength method of measuring path-averaged turbulent surface heat fluxes, J. Atmos. Ocean. Tech., 6, 280–292, 1989.

Andrews, L. C. and Phillips, R. L.: Laser Beam Propagation through Random Media, SPIE, Bellingham, Washington, USA, 2005.

Brion, J., Chakir, A., Charbonnier, J., Daumont, D., Parisse, C., and Malicet, J.: Absorption spectra measurements for the ozone molecule in the 350–830 nm region, J. Atmos. Chem., 30, 291–299, doi:10.1023/a:1006036924364, 1998.

Clifford, S. F.: Temporal-frequency spectra for a spherical wave propagating throught atmospheric turbulence, J. Opt. Soc. Am., 61, 1285–1292, 1971.

Consortini, A., Ronchi, L., and Stefanut, L.: Investigation of atmospheric turbulence by narrow laser beams, Appl. Optics, 9, 2543–2547, doi:10.1364/ao.9.002543, 1970.

De Bruin, H. A. R. and Evans, J. G.: Long path scintillometry: a brief review, in: Remote Sensing and Hydrology, edited by: Neale, C. M. U. and Cosh, M. H., IAHS Publication, Wallingford, UK, 180–183, 2012.

Ding, Y. H. and Liu, Y. J.: Analysis of long-term variations of fog and haze in China in recent 50 years and their relations with atmospheric humidity, Sci. China Ser. D, 57, 36–46, 2014.





ACPD
14, 21285–21314, 2014



Evans, J. G. and De Bruin, H. A. R.: The effective height of a two-wavelength scintillometer system, Bound.-Lay. Meteorol., 141, 165–177, doi:10.1007/s10546-011-9634-0, 2011.
Filho, F. C. M., Jayasuriya, D. A. R., Cole, R. S., and Helmis, C. G.: Spectral density of millimeter wave amplitude scintillations in an absorption region, IEEE T. Antenn. Propag., 31, 672–676, 1983.
Ishimaru, A.: Wave Propagation and Scattering in Random Media, Oxford University Press, New York, USA, 1997.
Järvi, L., Rannik, Ü., Mammarella, I., Sogachev, A., Aalto, P. P., Keronen, P., Siivola, E., Kulmala, M., and Vesala, T.: Annual particle flux observations over a heterogeneous urban area, Atmos. Chem. Phys., 9, 7847–7856, doi:10.5194/acp-9-7847-2009, 2009.
Lou, S., Liao, H., and Zhu, B.: Impacts of aerosols on surface-layer ozone concentrations in China through heterogeneous reactions and changes in photolysis rates, Atmos. Environ., 85, 123–138, doi:10.1016/j.atmosenv.2013.12.004, 2014.
Nebuloni, R.: Empirical relationships between extinction coefficient and visibility in fog, Appl. Optics, 44, 3795–3804, doi:10.1364/ao.44.003795, 2005.
Nieveen, J. P., Green, A. E., and Kohsiek, W.: Using a large-aperture scintillometer to measure absorption and refractive index fluctuations, Bound.-Lay. Meteorol., 87, 101–116, 1998.
Ott, R. H. and Thompson Jr., M. C.: Atmospheric amplitude spectra in an absorption region, IEEE T. Antenn. Propag., 16, 329–332, 1978.
Pant, P., Stalin, C. S., and Sagar, R.: Microthermal measurements of surface layer seeing at Devasthal site, Astron. Astrophys. Sup., 136, 19–25, 1999.
Rao, R.: Modern Atmospheric Optics, Science Press, Beijing, 2012.
Raut, J.-C. and Chazette, P.: Vertical profiles of urban aerosol complex refractive index in the frame of ESQUIF airborne measurements, Atmos. Chem. Phys., 8, 901–919, doi:10.5194/acp-8-901-2008, 2008.
Ripamonti, G., Jarvi, L., Molgaard, B., Hussein, T., Nordbo, A., and Hameri, K.: The effect of local sources on aerosol particle number size distribution, concentrations and fluxes in Helsinki, Finland, Tellus B, 65, 19786, doi:10.3402/tellusb.v65i0.19786, 2013.
Solignac, P. A., Brut, A., Selves, J. L., Beteille, J. P., and Gastellu-Etchegorry, J. P.: Attenuating the absorption contribution on $C_n^2$ estimates with a Large-Aperture Scintillometer, Bound-Lay. Meteorol., 143, 261–283, doi:10.1007/s10546-011-9692-3, 2012.
Stull, R. B.: An Introduction to Boundary Layer Meteorology, Kluwer Academic Publishers, Boston, USA, 1988.





ACPD
14, 21285–21314, 2014



Tatarskii, V. I.: Wave Propagation in a Turbulent Medium, McGraw-Hill Book Company Inc., New York, 1961.
van Dinther, D., Hartogensis, O. K., and Moene, A. F.: Crosswinds from a Single-Aperture Scintillometer using spectral techniques, J. Atmos. Ocean. Tech., 30, 3–21, doi:10.1175/jtech-d-12-00069.1, 2013.
Wang, T. I., Ochs, G. R., and Clifford, S. F.: Saturation-resistant optical scintillometer to measure $C_n^2$, J. Opt. Soc. Am., 68, 334–338, 1978.
William, H. P., Saul, A. T., William, T. V., and Brian, P. F.: Numerical Recipes the Art of Scientific Computing, 3rd Edn., Cambridge University Press, Cambridge, UK, 2007.
Wyngaard, J. C., Izumi, Y., and Collins, S. A.: Behavior of refractive-index-structure parameter near ground, J. Opt. Soc. Am., 61, 1646–1650, doi:10.1364/josa.61.001646, 1971.
Yuan, R., Zeng, Z., Xiao, L., Ma, C., Weng, N., and Wu, X.: Comparison of some methods of measuring refractive index structure parameter, Acta Optica Sinica, 20, 755–761, 2000.
Yuan, R., Sun, J., Luo, T., Wu, X., Wang, C., and Fu, Y.: Simulation study on light propagation in an anisotropic turbulence field of entrainment zone, Opt. Express, 22, 13427–13437, 2014.
Zhang, X., Huang, Y., Rao, R., and Wang, Z.: Retrieval of effective complex refractive index from intensive measurements of characteristics of ambient aerosols in the boundary layer, Opt. Express, 21, 17849–17862, doi:10.1364/oe.21.017849, 2013.





ACPD
14, 21285–21314, 2014



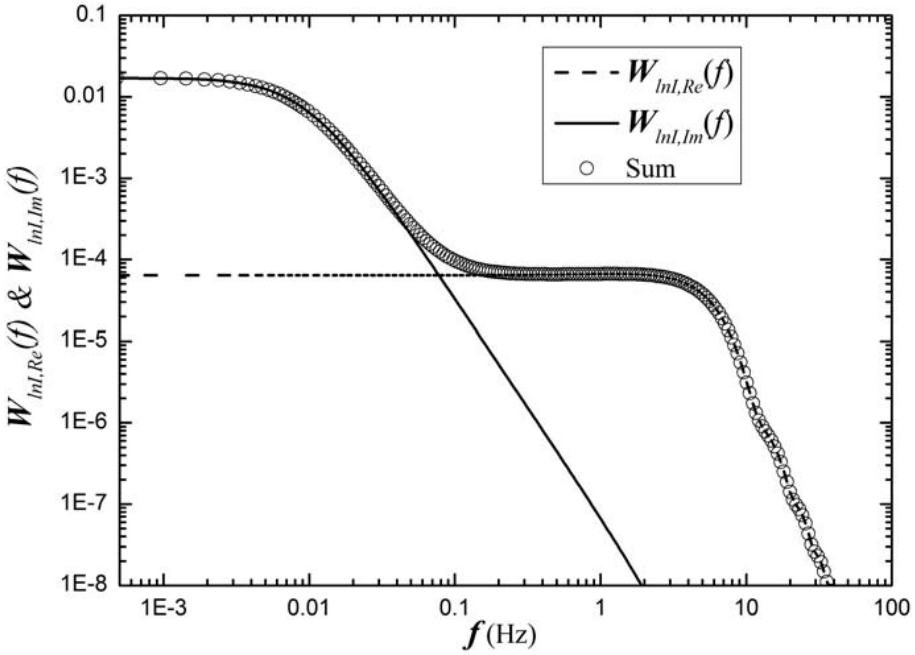


**Figure 1.** The theoretical temporal spectral density ($W_{\ln I,\mathrm{Re}}(f)$ and $W_{\ln I,\mathrm{Im}}(f)$) of the logarithmic light intensity fluctuations caused by the real and imagery parts of the refractive index (see text for parameter values used in the calculation).





ACPD
14, 21285–21314, 2014



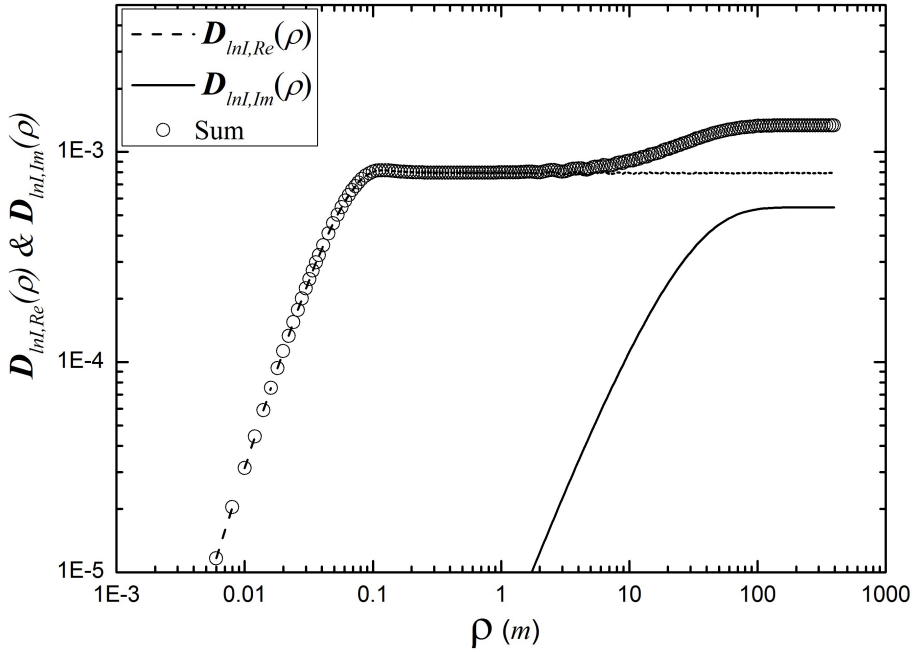


**Figure 2.** The calculated temporal structure function ($D_{\ln I,\mathrm{Re}}$ ($\rho$) and $D_{\ln I,\mathrm{Im}}$ ($\rho$)) of the logarithmic light intensity fluctuations caused by the real and imagery parts of the refractive index with the same parameters as Fig. 1.





ACPD
14, 21285–21314, 2014




**Figure 3.** Photographs of the measurement site **(a)** map of Hefei city, **(b)** Expanded view of the measurement sites in the USTC campus, which is marked with the rectangle in **(a)**. Point P in **(a)** indicates the site for visibility measurements, Points A and B in **(b)** shows the locations of the transmitter and receiver, respectively. Point C in **(b)** indicates the meteorological tower position. There are 4 heavy traffic roads surrounding the measurement site.





ACPD
14, 21285–21314, 2014



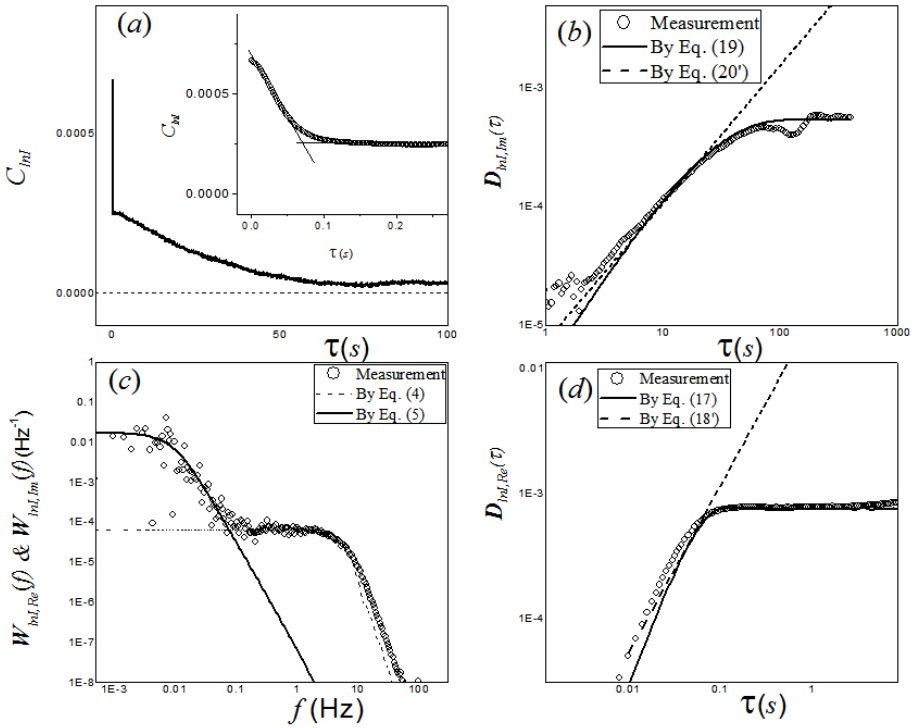


**Figure 4.** Parameters derived from a LAS observation example at 15 January 2014, 08:30 LT and comparison with theory. **(a)** Time-delay auto-correlation of the logarithmic light intensity fluctuations. **(b)** Structure function of the logarithmic light intensity fluctuations caused by the imagery part of the refractive index (circles) and the theoretical curves (solid line and dash line). **(c)** The temporal spectral density ($W_{\ln I,\mathrm{Re}}(f)$ and $W_{\ln I,\mathrm{Im}}(f)$) of the logarithmic light intensity fluctuations (circles) and the theoretical curves associated with the real and imagery parts of the refractive index (solid line and dashed line). **(d)** Structure function of the logarithmic light intensity fluctuations contributed by the real part of the refractive index (circles) and corresponding theoretical curves (solid line and dash line).





ACPD
14, 21285–21314, 2014



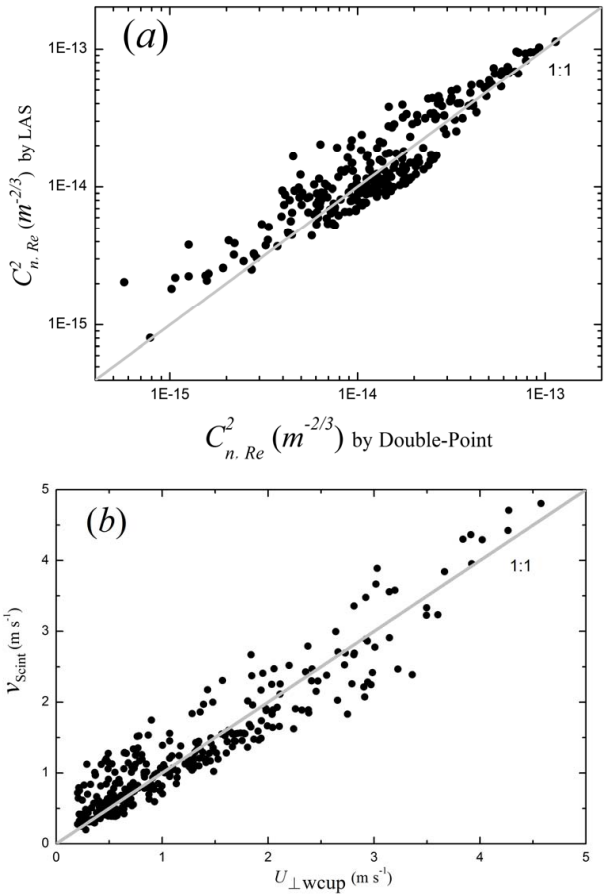


**Figure 5.** Comparisons of the real part of the ARISP and transverse wind speed between two methods. **(a)** Comparison of the real part of the ARISP between the Double-Point measurements and LAS measurements. **(b)** Comparison of transverse wind speeds between cup anemometer and LAS measurements.





ACPD
14, 21285–21314, 2014



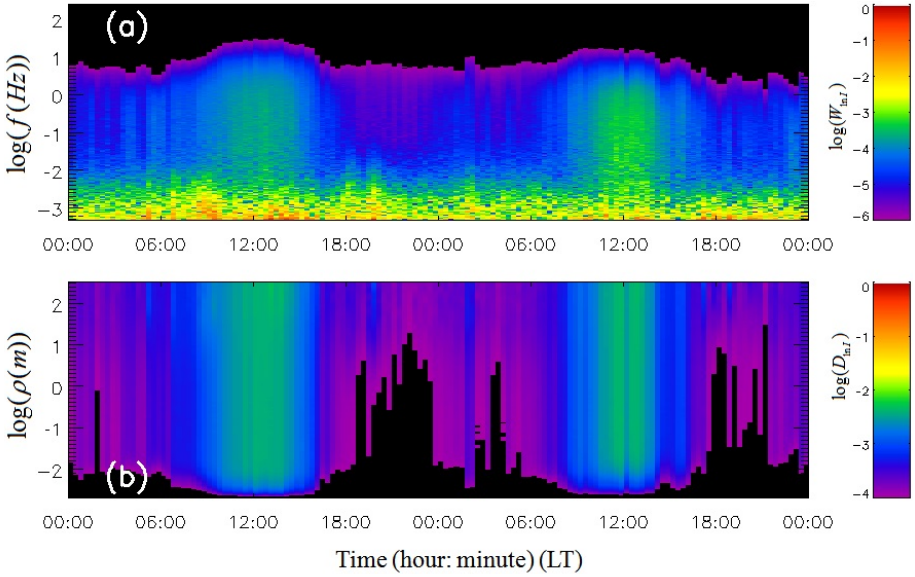


**Figure 6.** The evolution of the temporal spectral density **(a)** and structure function of the logarithmic light intensity fluctuations **(b)** during 15–16 January 2014. In **(a)** the two-dimensional color of contour denotes the logarithm of temporal spectral density of the logarithmic light intensity fluctuations according to the color bar at right. In **(b)** the two-dimensional color contour denotes the logarithm of structure function of the logarithmic light intensity fluctuations according to the color bar at right. The black grids indicate the values less than the minimum.





ACPD
14, 21285–21314, 2014



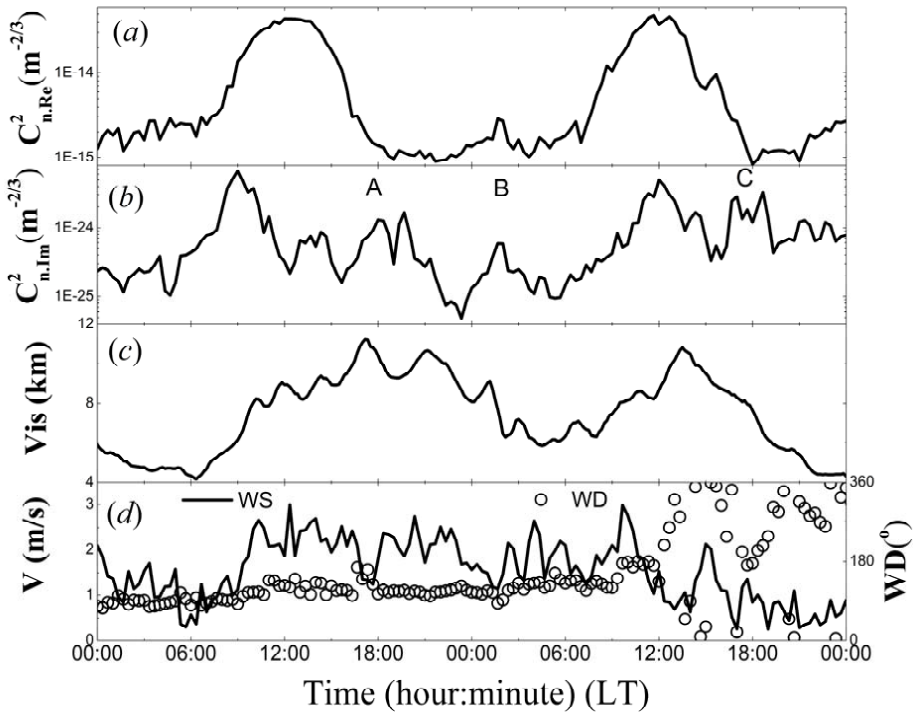


**Figure 7.** The temporal variations of the real part of the ARISP **(a)**, the imaginary part of the ARISP **(b)**, visibility **(c)**, and wind speed and direction **(d)** during 15–16 January 2014. A, B and C in **(b)** highlight three periods with large values for the imaginary part of the ARISP other than the two daily maximum. Details can be found in the text.





ACPD
14, 21285–21314, 2014